Dislocation detection of shield tunnel segments under non-uniform deformation conditions using RMLS point clouds

Ze You¹, Liying Wang¹

¹School of Geomatics, Liaoning Technical University, Fuxin 123000, China youze1997@163.com - ORCID 0009-0001-1899-0386 wangliyinglntu@163.com - ORCID 0000-0002-9338-1556

Keywords: Dislocation detection, Rail-borne mobile laser scanning, Segment joint location, Circumferential dislocation, Radial dislocation.

Abstract

Segment dislocation is a major issue in subway shield tunnels, and its detection is crucial for ensuring structural and operational safety. Existing methods often rely on local point clouds, failing to provide a comprehensive and precise representation of overall segment dislocation. Others assume an ideal cylindrical geometry, neglecting common non-uniform segment deformations. To address these limitations, we introduce a novel global deformation-aware approach for segment dislocation detection. The method first separates non-lining tunnel points to accurately reflect the tunnel lining structure and eliminate their adverse effects on segment joint extraction. This is achieved using an ellipse fitting residual statistics-based algorithm. Subsequently, circumferential joints are extracted and located by integrating adaptive intensity features with prior information, allowing the division of the tunnel lining into individual shield rings. Radial joints within each shield ring are then identified through a deep feature clustering algorithm. Finally, circumferential and radial dislocations are detected using a piecewise fitting approach for shield ring segments. The feasibility and effectiveness of the proposed method are verified using Rail-borne Mobile Laser Scanning (RMLS) point cloud data from Guangzhou Metro Line 8. Experimental results demonstrate that the method effectively detects dislocations under non-uniform deformation conditions, overcoming errors introduced by traditional methods that simplify segment geometry. Compared to conventional fault detection techniques, the proposed approach achieves improved accuracy and robustness.

1. Introduction

With accelerated urbanization and growing urban populations in China, infrastructure construction has experienced rapid expansion. Metro systems, serving as a critical solution to alleviate traffic congestion and improve urban mobility, have seen their tunnel construction scale up significantly. The shield tunnelling method, characterized by high automation, minimal environmental impact, and enhanced construction safety, has been widely adopted for precast segment assembly in metro tunnel engineering. Nevertheless, these prefabricated structures inevitably develop structural defects during long-term operations due to material aging, geological deterioration, and accumulated service time (Liu, 2020). Typical defects include segment dislocation, cracking, water leakage, and structural damage. Among these, segment dislocation stands out as one of the most critical issues, primarily arising from two mechanisms: (1) Relative displacement occurs when pressure differences between adjacent segments exceed the load-bearing capacity of connecting bolts; (2) Construction -related factors such as improper lining pressure control and substandard assembly quality during installation (Zhang, 2024). Dislocations directly induce tunnel convergence deformation and may trigger secondary defects like material spalling and water infiltration, severely compromising structural integrity and operational safety (Yin, 2023). Quantitative detection of segment dislocation serves as a vital indicator for assessing metro tunnel conditions, holding substantial practical significance for ensuring operational safety.

RMLS is a novel non-contact measurement technology. It obtains the 3D point cloud of the tunnel and laser reflection intensity information cross-section scanning. It offers technical advantages such as automation, digital acquisition high precision, and high density. The recorded spectral and spatial data contain detailed topology, geometry, texture, and structure information, providing a new technical approach for the

automatic global detection of tunnel segment dislocation. Subway shield tunnels have complex structures and are located underground, making them difficult to detect. These factors make it challenging to obtain spatial information. Accurately detecting tunnel dislocations becomes difficult. This information needs to cover the entire tunnel area and needs to be obtained efficiently from massive point clouds.

RMLS point cloud's methods for circumferential dislocation detection can be classified into three categories: (1) Curve-Fitting Comparative Method. This approach, as demonstrated by Yu (2021) extracts cross-sectional point clouds at predefined distances from the circumferential joint and projects them onto the tunnel's normal plane. For a target point (p), local point clusters from adjacent cross-sections undergo curve fitting to derive geometric parameters. The radial distance difference between two fitted curves defines the dislocation magnitude at p. While implemented in commercial software like Amberg Tunnel Cloud, its direct reliance on sectional point fitting amplifies noise sensitivity, constraining detection precision. (2) Plane-Fitting Comparative Methoddeveloped by Cui (2024), Bao (2023), and Guo (2023). This method fits planes to local point clusters (e.g., bolt-hole adjacent zones) on both sides of the circumferential joint. The distance between these fitted planes at the joint location quantifies the dislocation. Although effective for capturing deformations, its limited spatial sampling (localized data only) and its planar approximation of curved surfaces introduce systematic representation errors. (3) Several studies have used the Circle-Fitting Comparative Method (Xie, 2017; Zhao, 2020; Yue, 2021; Wang, 2022; Lu, 2022; Du, 2022). This technique performs circle fitting on cross-sectional point clouds extracted symmetrically about the circumferential joint. The radial offset between superimposed fitted circles determines dislocation magnitudes. However, its fundamental assumption of perfect circular tunnel geometry fails to account for non-uniform structural deformation, compromising accuracy in real-world applications.

Moreover, radial dislocation can be grouped into four types: (1) Plane-Fitting Comparative Method (Cui, 2024; Yu, 2021; Bao, 2023; Guo, 2023). This method fits planes to local point clusters on both sides of the radial joint. The distance between these fitted planes at the joint location serves as the radial dislocation measurement. (2) Point Spacing Methodcalculates the distance difference between edge points of adjacent segments at the radial joint to quantify radial dislocation (Yue, 2021). (3) Polar Radius Difference Method (Cui, 2019; Xie, 2023). Radial dislocation values derive from comparing polar radius differences between point clouds on both sides of the radial joint. (4) Arc-Fitting Comparative Method (Du, 2022; Xu, 2022; Zhang, 2024). This technique projects segment point clouds from both sides of the radial joint onto orthogonal xoz planes, generating 2D arcs. Subsequent circle fitting and distance measurement between arcs at the joint determine dislocation magnitudes. While methods (1)-(3) utilize localized point cloud data, they inherently suffer from representation errors due to limited spatial sampling. Method (4) avoids localized sampling limitations but introduces new errors by assuming ideal cylindrical geometry for tunnel segments, neglecting nonuniform structural deformation patterns.

This paper proposes the following contributions to address the above issues: (1) A 3D localization method for segment joints in elliptical shield tunnels based on point cloud data. As the raw format of RMLS data, the point cloud retains the complete 3D, geometric, topological, and intensity information. The method based on point cloud data effectively utilizes the available information in the point cloud, providing more accurate joint positioning results that are unaffected by tunnel ancillary facilities. Additionally, the joint location based on the point cloud provides an intuitive 3D representation, clearly showing the spatial location and distribution of joints and offering data support for segment dislocation analysis. (2) A segment dislocation detection method under non-uniform deformation is established. The method is based on the fact that the crosssectional shape of the circular tunnel Huang, 2022). The radial difference of the local elliptical curve is used to quantify the segment dislocation, which is determined from the segment's point cloud. It addresses the challenge of accurately segment dislocations detection under non-uniform deformation, improves fitting accuracy, and enables the prediction of shield tunnel deformation, providing an early warning for segment dislocations.

2. Description of experimental data

This study area is a tunnel section of Guangzhou Metro Line 8., The data was captured using the self-mobile intelligent laser scanning system independently developed by China Railway Design Group Co., Ltd. The laser scanner operates at a speed of 1 km/h (1×10^3 m / 3600 s = 0.28 m/s), and it performs 100 revolutions per second (corresponding to a scanning frequency of 100 sections per second). The subway tunnel contains cables, power supply equipment, natural gas pipelines, maintenance panels, lighting equipment, and other ancillary facilities. Each shield ring consists of 6 segments, including one capping block, two adjacent blocks, and three standard blocks, with a diameter D of 5.4 m and a shield ring width W of 1.5 m. The tunnel cross-section spacing is 2.8 mm. The number of point clouds in each cross-section is about 10160, and the corresponding point spacing is about $\pi \times 5.4$ m / 10160 = 1.6 mm.

Only data in the mileage interval from K25+440 to K25+450 of the north extension of Guangzhou Metro Line 8 are selected to validate the accuracy and feasibility of the proposed method, with a total of 22 shield rings and a total length of approximately 33.4 m and a total of 12014 profiles, as shown in Figure 1. The data are in LAS format, including 3D coordinates (x, y (mileage), z), laser reflectivity intensity, scanning line serial number, and other information. The 3D coordinate system is defined as follows: the origin O lies at the scanner center, the Y-axis points in the moving direction, the Z-axis points to the zenith, and the X-axis is perpendicular to the yoz plane. The axes in the 3D coordinate system satisfy the right-hand rule.

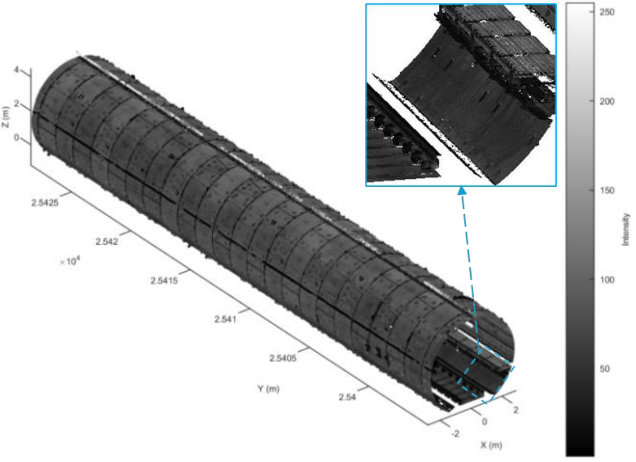


Figure 1. The experimental data.

3. Methodology

This research proposes an accurate method for segment dislocations detection in shield tunnels based on the RMLS point cloud. The original RMLS point cloud, which includes outliers, tunnel facilities (such as cables, power supply equipment, and natural gas pipelines), and tunnel linings, is subject to interference. First, a non-lining points elimination method based on ellipse-fitted residual statistics is introduced, utilizing the shape of the lining cross-section to separate nonlining points and avoid their interference with segment joint extraction and dislocation analysis. Thus, a 3D shield tunnel segment joint extraction and positioning method is designed. The method utilizes the intensity difference between the crosssections of the segment and the circumferential joint, combined with prior knowledge of the adjacent circumferential joint spacing, to extract and locate the circumferential joint, subsequently dividing the tunnel into several shield rings. Subsequently, the radial joint point cloud of each shield ring is extracted by utilizing the characteristic of the radial joint as a locally convex linear feature, enabling accurate segmentation of the tunnel . Finally, a segment dislocation detection method is developed for non-uniform deformation conditions detection. The method calculates the dislocation value by fitting the segment's curved surface. Figure 2 illustrates the detailed process of the proposed method, and the following sections provide a more in-depth explanation of the steps.

"Mobile Mapping for Autonomous Systems and Spatial Intelligence", 20–22 June 2025, Xiamen, China

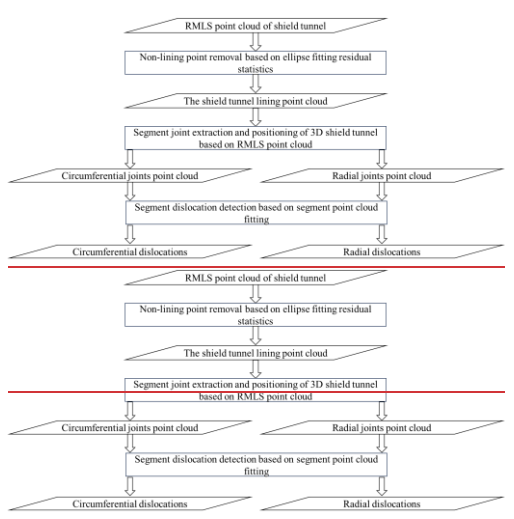


Figure 2. Flowchart of the proposed method.

3.1 Non-lining point removal based on ellipse fitting residual statistics

The segment joint lies on the surface of the tunnel lining, and the original RMLS point cloud contains both tunnel lining points and non-lining points. To prevent interference with subsequent methods, the non-lining point must first be removed. The cross-sections of shield tunnels are typically circular, but they are likely to deform into an elliptical shape over time. Therefore, an ellipse fitted to the cross-sectional point cloud is used to represent the tunnel lining cross-sections. Based on this, a non-lining point elimination method is designed, which relies on ellipse fitting residual statistics using the characteristic of non-lining points deviating from the tunnel lining noise. The specific steps are as follows:

(1) Tunnel lining cross-section ellipse fitted. Denote the given RMLS point cloud as:

$$P_{i} = \left\{ p_{i} \left(x_{i}, y_{i}, z_{i}, I_{i}, S_{i} \right), i = 1, ..., n_{i}, S_{i} = k, k = 1, ..., K \right\}$$
 (1)

method.

Where k = the index of the cross-section

i =the index of the laser point

 p_i = the *i*th laser point

 (x_i, y_i, z_i) = the coordinates of the *i*th laser point in the Cartesian coordinate system

 I_i = the intensity value of *i*th laser point

 S_i = the cross-section serial number of *i*th laser point

 n_k = the number of laser points of the kth crosssection.

Firstly, for each cross-section, the RANSAC ellipse-fitted method is used to determine the best fitting ellipse E_k and the fitting parameters are obtained, including the center of the ellipse $O_{k}=(X_k, Y_k, Z_k)$, the long half axis a_k , the short half axis b_k , focuses $F_k^1 = (\hat{x}_k^1, \hat{y}_k^1, \hat{z}_k^1), F_k^2 = (\hat{x}_k^2, \hat{y}_k^2, \hat{z}_k^2)$, as shown in Figure 3. To improve the accuracy of ellipse fitting, only the tunnel's cross-sectional point cloud of the upper part, which contains less noise, is used in the RANSAC ellipse fitting

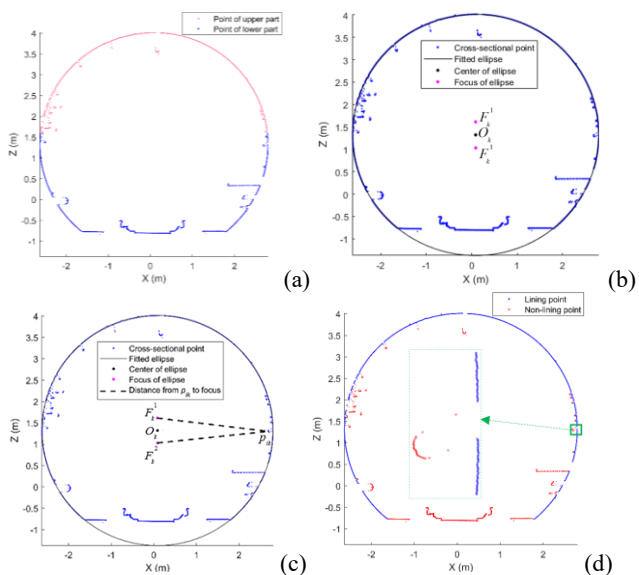


Figure 3. The kth cross-section ellipse-fitted and non-lining points removal. (a) Points of upper part and lower part; (b) Fitted ellipse and focus position; (c) Distance residuals from each point of the cross-section to the fitted ellipse; (d) Eliminated non-lining points.

(2) Non-lining points are eliminated based on ellipse-fitted residuals. The distance residuals from each section point to the fitted ellipse are calculated to form a residual set D_k .

$$\begin{cases}
D_k = \left\{ d_{ik}, i = 1, \dots, n_k \right\} \\
d_{ik} = \left\| \left[\left(x_i, y_i, z_i \right) - (\hat{x}_k^1, \hat{y}_k^1, \hat{z}_k^1) \right]_i + \left\| \left(x_i, y_i, z_i \right) - (\hat{x}_k^2, \hat{y}_k^2, \hat{z}_k^2) \right\|_i - 2a_k
\end{cases}$$

For $\forall d_{ik} \in D_k$, if $0 \le d_{ik} \le T_d$, the corresponding point is judged as the lining point; otherwise, the corresponding point is judged as the non-lining point and removed.

After the non-lining points removal, the obtained tunnel lining points are denoted as:

$$P_{k}' = \left\{ p_{i}(x_{i}, y_{i}, z_{i}, I_{i}, S_{i}), i' = 1, ..., n'_{k}, S_{i} = k \right\}$$
(3)

Where

k' = the index of the cross-section

i' = the index of the laser point

 $p_{i'}$ = the *i'*th laser point

 $(x_{i'}, y_{i'}, z_{i'})$ = the coordinates of i'th laser point in the Cartesian coordinate system

 $S_{i'}$ = the cross-section serial number of i'th laser point

 n_k = the number of laser points of the kth crosssection

3.2 Segment joint extraction and positioning of 3D shield tunnel based on RMLS point cloud

3.2.1 Circumferential joint extraction based on prior and adaptive intensity information: As illustrated in Figure 4(a), a significant intensity difference is observed between the segment and the circumferential joint. Figure 4(b) shows the cumulative intensity distribution of each cross-section. The analysis reveals that the cumulative intensity of the cross-section at each circumferential joint is significantly lower than that of the segments on either side, indicating a local minimum. Furthermore, the spacing between the circumferential joints of adjacent segments is fixed, precisely corresponding to the width of the shield ring. A circumferential joint extraction method combining prior knowledge and adaptive intensity information is introduced to address this. The specific steps are outlined below.

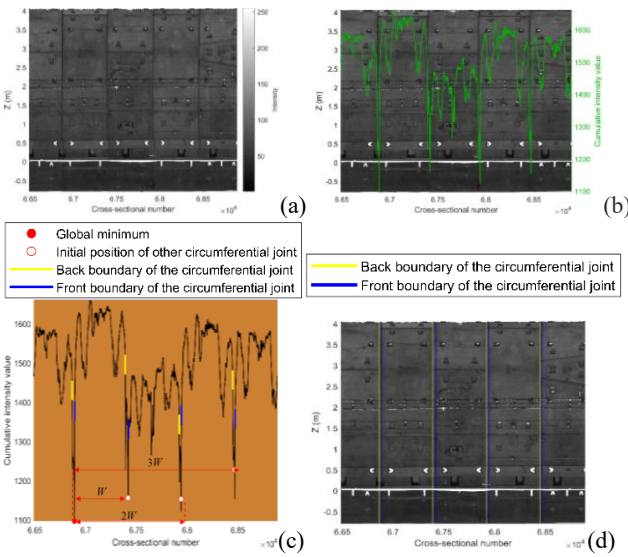


Figure 4. The method of circumferential joint extraction and positioning. (a) Side view of tunnel cross-sections; (b) Cumulative intensity value distribution of continuous cross-sections; (c) Initial positions of the circumferential joints and determination actual boundaries; (d) Extraction results of circumferential joints.

- (1) The circumferential joints are initially positioned using global intensity and prior information. First, the cumulative intensity of each cross-sectional point is calculated; thus, a cross-section feature set $\{m \mid m_1, ..., m_{K'}, ..., m_{K'}\}$ is formed, and the cross-section corresponding to the global minimum cumulative intensity $f_{\min}(m)$ is taken as the initial position of the circumferential joint $arg \ f_{\min}(m)$. Next, based on the fixed interval between adjacent circumferential joints, the cross-section at the initial position, with an interval of kW (where k is a non-zero integer multiplier), is used to determine the positions of the other circumferential joints. The initial positions of the circumferential joints are denoted by c_j , where j = 1, 2, ..., with j representing the number of circumferential joints, and $c_j = arg \ f_{\min}(m) \pm kW$, as shown by the red hollow circles in Figure 4(c).
- (2) Circumferential joint extraction based on adaptive local intensity analysis. As shown in Figure 4 (a), the circumferential joint in an actual tunnel typically has a certain width. Therefore, it is necessary to define the boundary of the cross-section on both sides of each circumferential joint to achieve accurate circumferential joint extraction. In order to adapt to the intensity of each circumferential joint and its segments on both sides,

first, according to Eq. (4), calculate the average value $\mu_j^L(\mu_j^R)$ and standard deviation $\sigma_j^L(\sigma_j^R)$ of the segment cross-sections from the Nth to the 2Nth segment located in the front (back) of the jth circumferential joint, $\mu_j^L - b \cdot \sigma_j^L$ and $\mu_j^R - b \cdot \sigma_j^R$ are used as indicators that deviate from the statistical characteristics of segment. N should be slightly larger than the number of cross-sections corresponding to the circumferential joints. Then, for the cross-section in $[c_j-N,c_j+N]$, the first cross-section with cumulative intensity less than $\mu_j^L - b \cdot \sigma_j^L$ and the last cross-section with cumulative intensity less than $\mu_j^R - b \cdot \sigma_j^R$ are searched and marked as c_j^L and c_j^R , respectively, The yellow line and the blue line in Figure 4(c) are shown. Here, b is a multiplier set to 3 according to the 3σ rule in the experiment. Finally, the cross-section in $[c_j^L, c_j^R]$ is marked as a circumferential joint, as shown in Figure 4(d).

$$\mu_{j}^{L} = \frac{\sum_{u=c_{j}-2N}^{c_{j}-N-1} m_{u}}{N} \quad \mu_{j}^{R} = \frac{\sum_{u=c_{j}+N+1}^{c_{j}+2N} m_{u}}{N} \quad \sigma_{j}^{L} = \sqrt{\frac{\sum_{u=c_{j}-2N}^{c_{j}-N-1} (m_{u}-\sigma_{j}^{L})}{N}} \quad \sigma_{j}^{R} = \sqrt{\frac{\sum_{u=c_{j}+N+1}^{c_{j}+2N} (m_{u}-\sigma_{j}^{R})}{N}}$$
(4)

3.2.2 Radial joint extraction based on deep feature clustering: The radial joint is characterized by its deviation from the tunnel lining surface and its specific length. Therefore, a radial joint extraction method based on deep feature clustering is introduced. First, the tunnel lining point cloud, after noise elimination, is segmented based on the ring joints described in Section 3.2.1, yielding the point cloud for each shield ring. Subsequently, each shield ring is treated as a processing unit. The depth feature is employed to quantify the degree of deviation of the laser points from the shield ring cross-section. Cluster analysis is then conducted on the local depth maxima to determine the initial position of the radial joint. Finally, buffer analysis is employed to refine the extraction of the radial joint within the shield ring. The specific steps are detailed as follows.

(1) Quantification of the tunnel lining surface deviation using depth features. As shown in Eq. (5), each cross-section of the shield ring is analyzed sequentially. The tunnel cross-section, referred to as the standard ellipse E_k , is characterized by the fitted ellipse derived from the lining point cloud P_K' . The distance $d_{i'k}$ between each lining point and the standard ellipse is utilized as the depth feature D_K' .

$$\begin{cases}
d_{r_k} = \left\| \left(x_{r_k}, y_{r_k}, z_{r_k} \right) - (\hat{x}_k^1, \hat{y}_k^1, \hat{z}_k^1) \right\|_2 + \left\| \left(x_{r_k}, y_{r_k}, z_{r_k} \right) - (\hat{x}_k^2, \hat{y}_k^2, \hat{z}_k^2) \right\|_2 - 2a_k \\
D_k' = \left\{ d_{r_k} \mid i' = 1, ..., n_k' \right\}
\end{cases}$$
(5)

where $(x_{i'k}, y_{i'k}, z_{i'k})$ is the *i*th point coordinate in the *k*th cross-section of lining point cloud.

(2) The initial position of the radial joint is identified through clustering of local depth maximum. Compared with the adjacent segments, the radial joints deviate from the standard ellipse, and the depth feature exhibits a local maximum. As illustrated in Figure 5, the depth information of the noise-free point cloud within the kth cross-section is presented. The horizontal axis represents the polar angle θ of the discrete noise-free point cloud, which can be derived from the Cartesian coordinates of the points using Eq. (6).

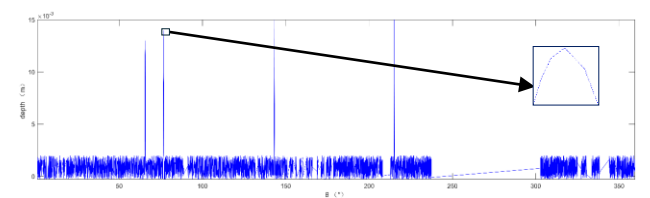


Figure 5. The depth information expansion diagram of the lining points for the kth cross-section.

$$\theta_{i'k} = \arctan\left(\frac{z_{i'k} + X_k}{x_{i'k} + Z_k}\right) \tag{6}$$

Here, $\theta \in (0,2\pi)$, (X_k, Z_k) represents the translation distance between the ellipse and the laser scanning centers. Therefore, the local maximum positioning method is used to locate the local maxima in each cross-section. Accordingly, nearest neighbor clustering is performed on the local extreme points (the method is shown in Figure 6). The clustering results are shown in Figure 7. Furthermore, the radial joint has a certain length. The length of each clustering result in the y direction is measured. If this length is greater than or equal to the shield ring width, the initial position of the corresponding radial joint is determined.

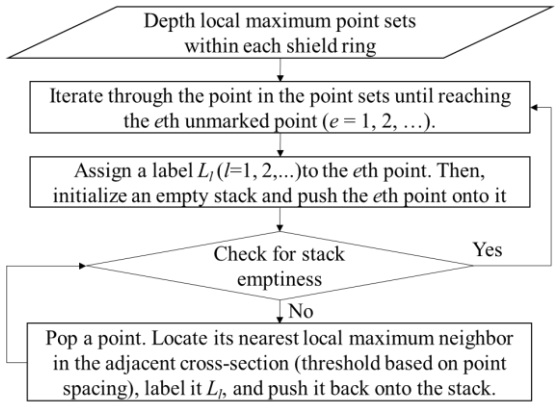


Figure 6. The clustering method of local maximum points.

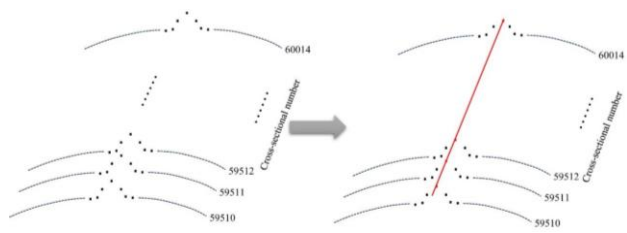


Figure 7. The clustering result of the local maximum points for a radial joint.

(3) Radial joint extraction under buffer analysis. The buffer zone is defined using the initial position of each radial joint as the center and the specified buffer distance. Based on this, as shown in Figure 8, the point cloud within the same buffer, where the depth value exceeds 0, is identified as the radial joint point cloud.

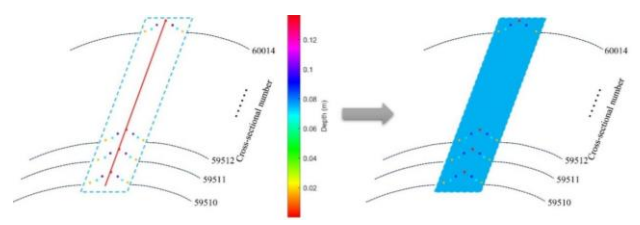


Figure 8. The clustering result of the local maximum points for a radial joint.

3.3 Segment dislocation detection based on segment point cloud fitting

3.3.1 Circumferential dislocation detection based on piecewise fitting analysis: The circumferential dislocation indirectly indicates the safety state of the tunnel's longitudinal structure. The traditional method directly applies global RANSAC ellipse fitting to the cross-sections on both sides of the circumferential joint to reflect overall deformation. However, since a single shield ring consists of multiple segments, this method can not fully match each segment, preventing an accurate reflection of detailed deformation. To address these issues, a novel circumferential dislocation detection method is proposed. First, two adjacent shield rings are extracted based on the circumferential joints described in Section 3.2.1. The point cloud within 10 to 15 cm from the circumferential joint of the two shield rings are intercepted as the piece data a and b. Then, as shown in Figure 9, based on the radial joints identified in Section 3.2.2, the front and back piece data a and b are decomposed into independent segments. Ellipse fitting is applied to the front and back piece data according to the segment positions. This process yields the ellipse-fitted parameters, along with the starting and ending angles for each segment. The position of the segment corresponding to the shield ring on the xoz projection surface is calculated according to the interval of 1°, statistical displacement distance, the maximum dislocation, the starting and ending angles of the dislocation are marked in red.

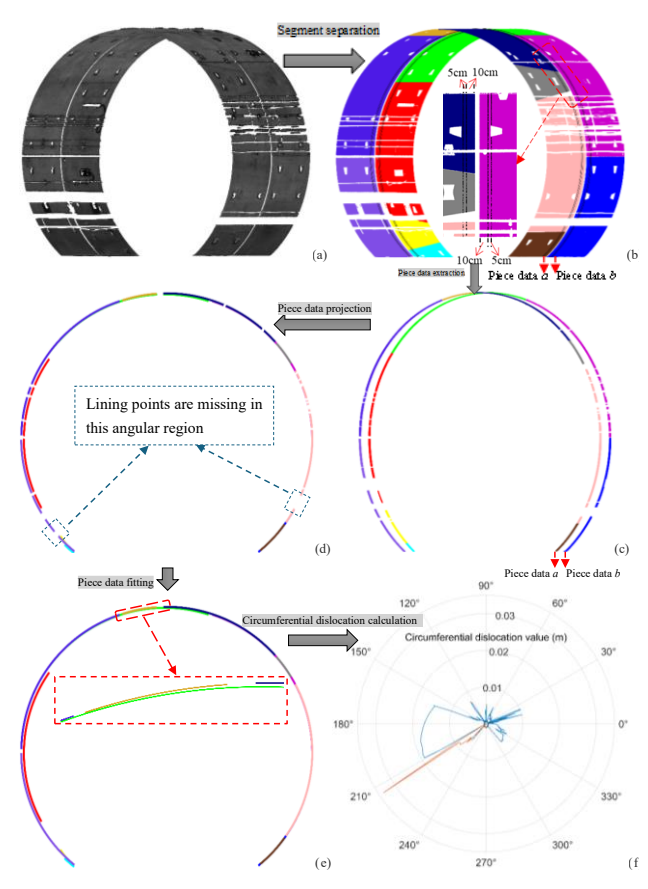


Figure 9. The circumferential dislocation detection process. (a) Two adjacent shield rings; (b)Segment separation result; (c) The piece data a and b extraction; (d)The piece data a and b projection; (e) The elliptical arc after fitting; (f) The detected circumferential dislocation.

3.3.2 Radial dislocation detection based on fitted segment elliptical arc: The radial dislocation can detect the non-uniform stress in the local part of the tunnel (i.e., a single shield ring) and promptly issue an early warning. In this research, the radial dislocation of each shield ring is calculated based on the segmented curve fitting method, the located radial joints, and the segmented segments. In the designed circular shield tunnel, each segment is part of the standard cylinder. Due to the influence of external load and train vibration, the lining structure of the operating tunnel undergoes slight uneven deformations, forming an elliptical cylinder (Huang, 2022). Therefore, the 2D arc formed by projecting the segment point cloud onto the xoz plane is part of the elliptic curve. Based on the above theory, the segments on both sides of the radial joint are first projected onto the xoz plane, and the RANSAC ellipse fitting method is used to fit each arc. Furthermore, the distance difference between the two arcs at the joint is calculated to obtain the dislocation value between the segments, as shown in Figure 10.

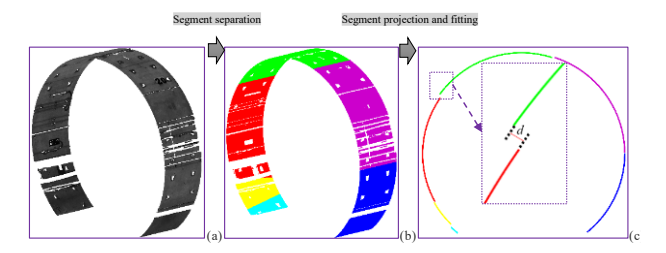


Figure 10. Calculation method of radial dislocation. (a) Shield ring; (b) The shield ring after segment separation; (c) Calculate the distance difference of the elliptical arc at the radial joint.

4. Experimental results and discussion

The original point cloud obtained in Section 2 is 122,027,603 points. The ellipse fitting residual analysis method proposed in Section 3.1 is used to detect and eliminate nonlining points such as abnormal scanning points, tunnel ancillary facilities, and tunnel track facilities to avoid subsequent interference with circumferential and radial dislocation detection. First, the upper part of each cross-section determines the best-fitted 3D ellipse by an ellipse fitting method based on the RANSAC technique. Then, the residual value between each cross-section point and the fitted ellipse is calculated. If the residual value is less than 0 or greater than the residual threshold T_d , the corresponding cross-section points are regarded as noise points and removed. In the experimental point cloud, the actual girth depth is 0.12 m. So, T_d is set to 0.12 m. The removal results of non-lining points of the experimental tunnel point cloud are shown in Figure 11.

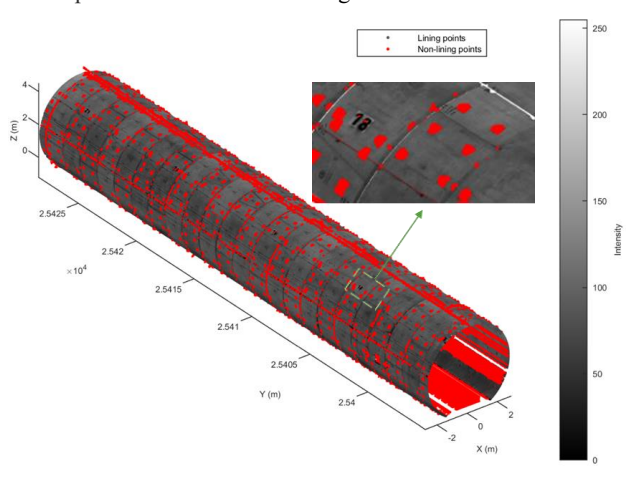


Figure 11. The non-lining points removal result.

The visualization results in Figure 11 demonstrate that the non-lining points are effectively eliminated using the proposed circular fitting residual-based method, and the remaining lining points can accurately reflect the tunnel structure. The tunnel point cloud is reduced to 65,275,528 points by non-lining point removal processing. Based on the tunnel lining point cloud obtained in Figure 11, the Circumferential joint extraction method proposed in Section 3.2, which combines prior and adaptive intensity information, is used to locate the Circumferential joint cross-section. The positioning results of the Circumferential joints are shown in Figure 12, along with detailed information for one circumferential joint.

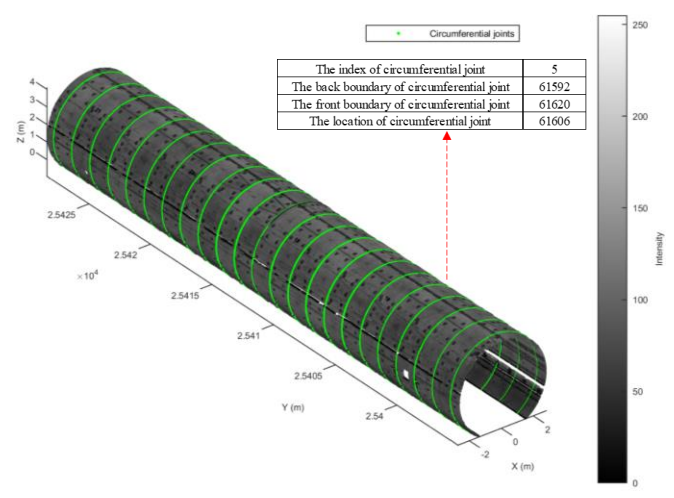


Figure 12. The result of circumferential joints extraction and positioning.

Based on the circumferential joints obtained in Figure 12, the tunnel lining is divided into various shield rings, and the radial joints are located by the radial joint extraction method based on depth feature clustering in Section 3.2.2. The results shown in Figure 13 demonstrate that the method can accurately extract all the points representing radial joints, with performance nearly comparable to manual labelling. Even if the radial joints are blocked by wires, power lines, or their brackets, this may interfere with the positioning and extraction of radial joints. However, the proposed method can still accurately locate them.

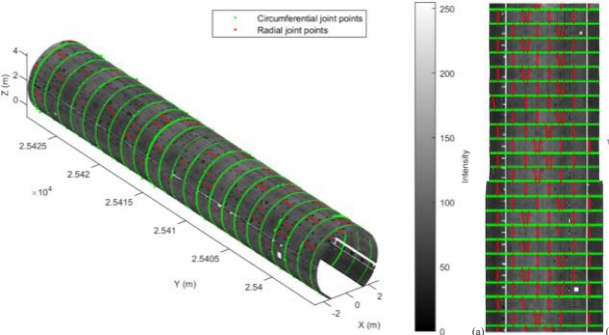


Figure 13. The results of radial joints extraction. (a) 3D view; (b) 2D unfolded view along the central axis.

Based on the Section 3.2 method, the shield ring is divided into various segments by the position of the circumferential joints and the radial joints in Figure 13. Using the circumferential dislocation detection method in Section 3.3.1, the results of each circumferential dislocation are analyzed, including the maximum of dislocation, the maximum angle of dislocation, the starting angle and the ending angle (see Table 1). Figure 14 shows the variation trend of circumferential dislocation at different angles. The orange curve range of the small graph in Figure 14 represents the angle range in Table 1, and the highest value of the curve represents the amount of dislocation in Table 1. Figure 14 shows the variation trend of circumferential dislocation at different angles. The orange curve range of the small graph in Figure 14 represents the angle range in Table 1, and the highest value of the curve represents the amount of dislocation in Table 1.

The index of	The maximum	C	The starting	The ending
the	of the	location of the	angle of the	angle of the
circumferential	circumferential	circumferential	circumferential	circumferential
dislocation	dislocation (m)	dislocation (°)	dislocation (°)	dislocation (°)
1	0.00389	159	149	161
2	0.00365	136	123	138
3	0.01020	159	101	182
4	0.00146	192	191	202
5	0.00280	131	122	137
6	0.00951	173	171	205
7	0.01038	178	177	179
8	0.00647	178	176	179
9	0.00631	137	116	155
10	0.00367	288	272	303
11	0.00871	271	270	286
12	0.01407	195	174	207
13	0.00790	131	129	148
14	0.00674	97	66	124
15	0.01151	204	202	206
16	0.00737	195	185	201
17	0.00440	288	277	296
18	0.01146	288	287	290
19	0.01048	173	172	174
20	0.01061	157	71	174
21	0.00555	173	138	176
22	0.00804	152	109	168
23	0.01193	0	354	17

Table 1. Circumferential dislocations information.

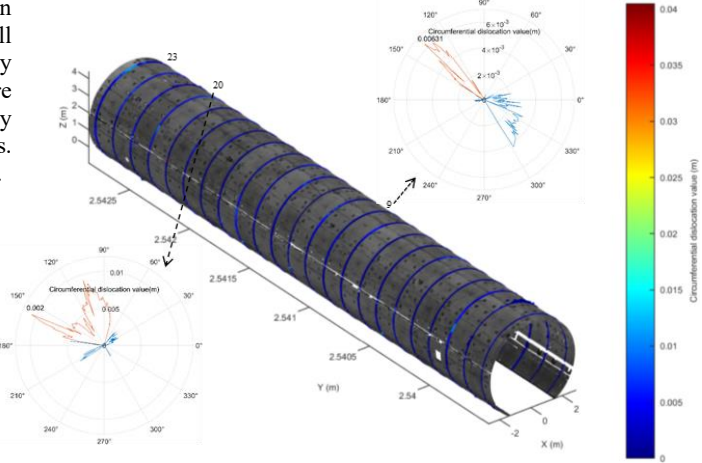


Figure 14. 3D view for the detected circumferential dislocations.

According to the 9.3.5 provisions on the allowable deviation and inspection method of segment assembly in the 'Shield Tunnel Construction and Acceptance Specification '(GB 50446-2017) and the 16.0.5 provisions on the allowable deviation of the tunnel (as shown in Table 2), the circumferential dislocation in the experimental area is analyzed. The results demonstrated that the circumferential dislocation of the experimental area complies with China's national standards, with no abnormal area detected. Figure 14 shows the angle interval variation diagram of the 4-th and 20-th circumferential dislocations in the experimental area, and the magnification details of the diagram further prove that the circumferential dislocation control in the experimental area is reasonable.

Dislocation type	Allowable deviation during the assembly stage (m)	Allowable deviation during the operational stage (m)
Radial dislocation	0.005	0.010
Circumferential dislocation	0.006	0.015

Table 2. The allowable maximum dislocation of subway shield tunnel.

To verify whether the proposed circumferential dislocation detection method achieves higher accuracy than traditional approaches, we compared it with Du, 2022. Their method extracts multiple cross-sectional point sets from both sides of the circumferential joint, applies Taubin circle fitting to determine cross-sectional centers, resamples points (retaining one per angular interval), and projects them onto the xoz plane. Circumferential dislocation is calculated as the distance difference between corresponding angular points across the circumferential joint. Results from multiple datasets are averaged to enhance precision. Table 3 shows that while most detected dislocation angles align with those in Table 1, discrepancies exist (marked in purple) where missing lining points at specific angles create incomplete coverage. This prevents identifying the true maximum circumferential dislocation position. In contrast, our method achieves full lining-covered regions, angular coverage across all demonstrating a key advantage. Significant differences in maximum circumferential dislocation values appear between the two methods (Tables 1 and 3). Conventional results frequently exceed tolerance limits (red values in Table 3) due to center positioning errors from global cross-sectional fitting. As Figure 15 illustrates, these errors propagate into dislocation calculations, particularly under non-uniform deformation. Our approach adapts better to segment deformation irregularities, ensuring higher accuracy for practical engineering applications. This comparison confirms the proposed method's superiority in complex shield tunnel monitoring scenarios.

The index of the	The maximum of the	The angular location of		
circumferential	circumferential	the circumferential		
dislocation	dislocation (m)	dislocation (°)		
1	0.00797	1 <u>5</u> 9		
2	0.02220	<mark>36</mark>		
3	0.02111	<mark>59</mark>		
4	0.01104	192		
5	0.00820	<mark>160</mark>		
6	0.00981	173		
7	0.00979	178		
8	0.01026	178		
9	0.01994	337		
10	0.01464	288		
11	0.01847	271		
12	0.01334	195		
13	0.01835	131		
14	0.01750	197		
15	0.01629	204		
16	0.02314	195		
17	0.01881	288		
18	0.02304	288		
19	0.01280	203		
20	0.01230	157		
21	0.01159	173		
22	0.02133	152		
23	0.01343	290		
23	0.01343	290		

Table 3. Circumferential dislocations information by Du ,(2022).

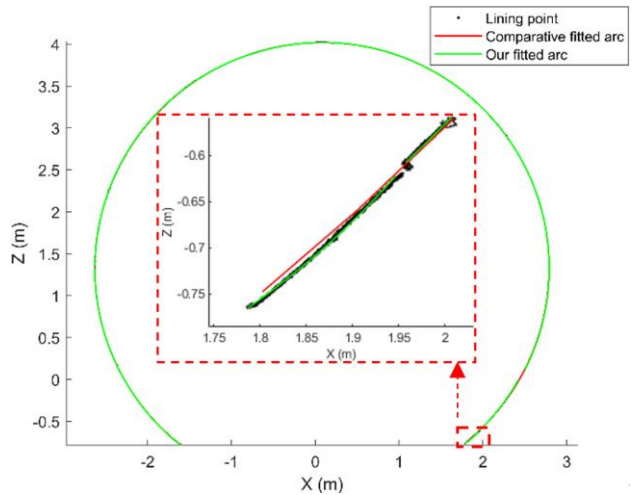


Figure 15. 3D view for the detected circumferential dislocations.

Following the same approach, radial dislocation across individual rings was analyzed using the segmented ellipse fitting-based radial dislocation detection method from Section 3.3.2, implemented on tunnel segments partitioned by circumferential joints and radial joints. The results (Table 4) and Figure 16 demonstrate the radial dislocation variation trends at different positions.

The index of the shield	Radial dislocation amount (m)				
ring					
1	0.00539 0.00072 0.00149 0.00366 0.00080	Nan			
2	0.01170 0.01413 0.03207 0.00330 Nan	Nan			
3	0.00450 0.00944 0.00091 0.00189 0.00104	Nan			
4	0.00469 0.00729 0.01564 0.01027 0.00140	Nan			
5	0.000210.000670.002060.007820.00236	Nan			
6	0.00356 0.00991 0.00346 0.00313 0.00521	Nan			
7	0.00862 0.00927 0.00296 0.00829 Nan	Nan			
8	0.00361 0.01144 0.00473 0.00235 0.00554	Nan			
9	0.00820 0.00454 0.00787 0.00654 0.00320	Nan			
10	0.01048 0.00297 0.00056 0.00096 Nan	Nan			
11	0.01009 0.00287 0.00755 0.01434 Nan	Nan			
12	0.00091 0.00240 0.00069 0.00068 0.00177	Nan			
13	0.00653 0.00565 0.00478 0.01279 0.00565	Nan			
14	0.00626 0.00088 0.00197 0.00034 0.00505	0.00661			
15	0.00249 0.00167 0.00121 0.00122 Nan	Nan			
16	0.01567 <mark>0.01160</mark> 0.003590.00565 Nan	Nan			
17	0.00492 0.00484 0.00933 0.00716 Nan	Nan			
18	0.00234 <mark>0.01030</mark> 0.005850.004490.00366	Nan			
19	0.00006 <mark>0.02361</mark> 0.018550.00175 Nan	Nan			
20	0.00378 0.00598 0.00121 0.00526 0.00312	Nan			
21	0.005320.00071 <mark>0.02017</mark> 0.00128 Nan	Nan			
22	0.00149 0.00754 <mark>0.01524</mark> 0.00709 0.0063	Nan			

Table 4. Radial dislocations information.

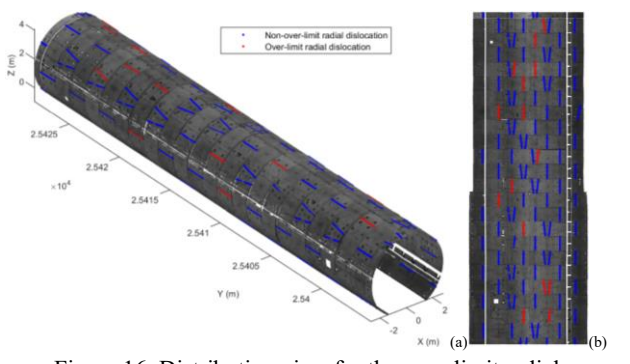


Figure 16. Distribution view for the over-limit radial dislocations. (a) 3D view; (b) 2D unfolded view along the central axis.

According to Table 2, 'Metro Shield Tunnel Allowable Deviation Specification', the radial dislocations of the following shield rings in the experimental area exceed the specified limits: No. 1 and No. 2 of the 2nd shield ring, No. 3 and No. 4 of the 4th shield ring, No. 2 of the 8th shield ring, No. 1 of the 10th shield ring, No. 1 and No. 4 of the 11th shield ring, No. 4 of the 13th shield ring, No. 1 and No. 2 of the 16th shield ring, No. 2 of the 18th shield ring, No. 2 and No. 3 of the 19th shield ring, and No. 3 dislocation of the 21st and 22rd shield rings (see Figure 16(b)). It is recommended that the operating unit immediately inspect the excessive radial dislocations and formulate timely disposal measures to eliminate hidden dangers and prevent accidents.

To validate the superior fitting accuracy of the proposed radial dislocation detection method compared to conventional approaches, we further compared it with the corresponding algorithm from Du, (2022). Their method employs segmented circle fitting for radial dislocation detection, and the results are presented in Table 5.

The index of the	Radial dislocation amount (m)					
shield ring	` '					
1	0.00539	0.00072	0.00151	0.00454	0.00081	Nan
2	0.0117	0.01256	0.03282	0.00393	Nan	Nan
3	0.0045	0.00937	0.00096	0.00101	0.00104	Nan
4	0.00469	0.00729	0.01556	0.00991	0.00140	Nan
5	0.00021	0.00077	0.00198	0.00725	0.00236	Nan
6	0.00356	0.00991	0.0034	0.00306	0.00521	Nan
7	0.00861	0.00915	0.00348	0.00408	Nan	Nan
8	0.00359	0.01144	0.00461	0.00764	0.0127	Nan
9	0.00819	0.0047	0.00774	0.00495	0.00320	Nan
10	0.01048	0.00297	0.0011	0.00145	Nan	Nan
11	0.00911	0.00297	0.0068	0.00241	Nan	Nan
12	0.00091	0.00225	0.00074	0.00189	0.00177	Nan
13	0.00653	0.00566	0.0047	0.01016	0.00565	Nan
14	0.00596	0.00089	0.00209	0.00038	0.00505	0.00661
15	0.00212	0.00138	0.00121	0.00138	Nan	Nan
16	0.01567	0.01158	0.00032	0.00936	Nan	Nan
17	0.00514	0.00466	0.00933	0.00707	Nan	Nan
18	0.00234	0.0103	0.00564	0.00292	0.00366	Nan
19	0.00023	0.02346	0.01855	0.00169	Nan	Nan
20	0.00378	0.00597	0.00104	0.00651	0.00312	Nan
21	0.00512	0.00055	0.02033	0.0012	Nan	Nan
22	0.00149	0.00754	0.01508	0.00825	0.0063	Nan

Table 5. Radial dislocations information by Du, (2022).

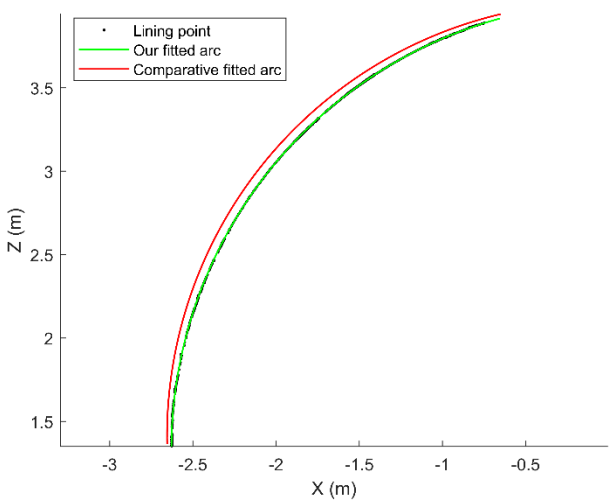


Figure 17. Between our fitted arc and comparative fitted arc.

The comparison reveals that most radial dislocation values align closely with Table 3 results (green values in Table 4). However, three cases show missed detections (red values in Table 4), and one false alarm occurs (purple value in Table 4). These

limitations stem from inherent flaws in the circular fitting method: Oversimplified geometry representation: The method oversimplifies segment geometry, reducing sensitivity to localized deformations (Figure 17), leading to missed detections under non-uniform deformation. Noise susceptibility: Irregular fitting caused by noise interference triggers false alarms.

In contrast, the proposed method better captures deformationinduced shape variations, achieving tighter alignment with actual segment geometry. This enables precise detection of subtle yet critical radial dislocation and timely warnings for problematic cases under non-uniform deformation. These results demonstrate dual advantages in temporal responsiveness and measurement accuracy.

5. Conclusions

To inspect and analyze the segment dislocations of subway shield tunnels under non-uniform deformation conditions, a detection method based on RMLS point clouds is proposed. First, a proposed ellipse-fitted residual method is used to detect and remove non-lining points in the tunnel point cloud that could interfere with subsequent segment joint extraction. Then, using the 3D tunnel segment circumferential and radial joint extraction and positioning method proposed in this work, the shield ring, circumferential joint, and radial joint are successfully located and separated. Finally, a segment dislocation detection method is developed for non-uniform deformation conditions. The method calculates the dislocation value by fitting the segment's curved surface. The method successfully calculates the circumferential and radial dislocation values, analyzes the dislocations, and warns of excessive dislocations. The accuracy and feasibility of this method are verified using the experimental point cloud from the K25 + 440 ~ K25 + 450 mileage interval of the north extension line of Guangzhou Metro Line 8. After analysis, the circumferential dislocation does not exceed the limit, but 16 radial dislocations exceed the limit and must be addressed promptly to avoid accidents. Compared to the traditional method, it has higher reliability. The proposed method is intended solely for segment joint extraction and localization in circular tunnels, and modifications are needed for other shapes, such as rectangular and double-O tunnels. For other geometric shapes, appropriate modifications can be made in Section 3.1. Firstly, different segments can be determined by the angle between the adjacent front and rear points of the section. If it is a straight line, a straight line is used for fitting, and other shapes are similarly fitted; as for the subsequent operation is similar.

Acknowledgements

The completion of this research was supported by multiple funding sources and resource projects. This work was partially funded by the National Natural Science Foundation of China (Grant Nos. 42571520 & 42201482), partially by the 2024 Joint Fund Project of Liaoning Provincial Natural Science Foundation (Grant No. 20240315) and also supported by the GPU Resource Support Project of Liaoning Technical University. We would like to express our sincere gratitude to the above funding agencies and supporting projects.

References

China Urban Rail Transit Association, 2024: Urban rail transit 2023 annual statistics and analysis report interpretation. China Metros, 2024, (4): 15-17. doi:10.14052/j.cnki.china.metros. 2024.04.012.

Zhiwei Zhang, Gang Zheng, Xuesong Cheng, Rongzhu Liang, Changjie Li, Zhiwu Zhong, Jing Zhao, 2024: Analytical approach for longitudinal deformation of shield tunnels considering bending-shear-torsional effects of circumferential joints. Tunnelling and Underground Space Technology, 152,105946. doi.org/10.1016/j.tust.2024.105946.

Tingjin Liu, Siwei Chen, Hongyuan Liu, 2020: Deformation characterisation and distress diagnosis of a metro shield tunnel by adjacent constructions. Advances in Civil Engineering, 4216349: 1-17. doi.org/10.1155/2020/4216349.

Ziren Yin, Zhanzhan Lei, Ao Zheng, Jiasong Zhu, Xiao-Zhou Liu, 2023: Automatic detection and association analysis of multiple surface defects on shield subway Tunnels. Sensors, 23(7106). doi.org/10.3390/s23167106.

Yuxian Zhang, Xuhua Ren, Jixun Zhang, Zichang Ma, 2024: A Method for Deformation Detection and Reconstruction of Shield Tunnel Based on Point Cloud. Journal of Construction Engineering and Management, 150(3): 1-13. doi:10.1061/JCEMD4.COENG-14225.

Qiang Zhang, Yifan Chen, 2023: Monitoring method of segment dislocation in shield tunnel joint assembly. URBAN ROADS BRIDGES & FLOOD CONTROL, 294(10): 261-264.

Dawei Huang, Hao Jiang, Changjie Xu, Wenbo Tu, Xue Li, Wei Wang, 2022: A new design method of shield tunnel based on the concept of minimum bending moment. Applied Sciences, 12(3): 1082. doi.org/10.3390/app12031082.

Xiongyao Xie, Xiaozhi Lu, 2017: Development of a 3D modeling method for tunnel deformation monitoring based on terrestrial laser scanning. Underground Space, 2: 16-29. doi.org/10.1016/j.undsp.2017.02.001.

Jianjun Lu, Wenhai Li, Zhanglin Yan, Yan Bao, Xu Wu, Shuxin Ni, 2022: Circumferential seam detection and analytics of segment misplacement between rings of subway shield tunnels based on featured point cloud of bolt holes. Bulletin of Surveying and Mapping, 2022(9): 06-11. doi:10.13474/j.cnki.11-2246.2022.0255

Zixuan Wang, 2022: Automatic extraction of dislocation of the circular shield tunnel segment based on moving scanning point cloud. Geotechnical Investigation & Survey, 50(09): 60-65. doi.org/10.1016/j.autcon.2019.102889.

Yabo Zhao, Zhi Wang, 2020: Analysis and application study of tunnel segment stagger based on mobile 3D scanning technology. Bulletin of Surveying and Mapping, 2020(8): 160-163. doi:10.13474/j.cnki.11-2246.2020.0271.

Zeyu Yue, Haili Sun, Ruofei Zhong, Liming Du, 2021: Method for tunnel displacements calculation based on mobile tunnel monitoring system. Sensors, 13(4407). doi.org/10.3390/s21134407

Liming Du, Ruofei Zhong, Haili Sun, Yong Pang, You Mo, 2022: Dislocation detection of shield tunnel based on dense cross-sectional point clouds. IEEE Transactions on Intelligent Transportation Systems. 2022, 3156385. doi: 10.1109/TITS.2022.3156385.

Hao Cui, Qingzhou Mao, Jian Li, Qingwu Hu, Yiwen Tao, Jie Ma, 2024: Shield tunnel dislocation detection method based on

semantic segmentation and bolt hole positioning of MLS point cloud. IEEE Transactions on Geoscience and Remote Sensing, 62(5702815): 1-15. doi:10.1109/TGRS.2024.3386308.

Lei Xu, Jian Gong, Jiaming Na, Yuanwei Yang, Zhao Tan, Norbert Pfeifer, Shunyi Zheng, 2022: Shield tunnel convergence diameter detection based on self-driven mobile laser scanning. Remote Sciences, 2022, 14(767). doi.org/10.3390/rs14030767

H. Cui, Xiaochun Ren, Wei Wang, 2019: Shield subway tunnel deformation detection based on mobile laser scanning. Automation in Construction, 106(102889): 1-12. doi.org/10.1016/j.autcon.2019.102889.

Anbin Yu, Wensheng Mei, Mulin Han, 2021: Deep learning based method of longitudinal dislocation detection for metro shield tunnel segment. Tunnelling and Underground Space Technology, 113(103949). doi.org/10.1016/j.tust.2021.103949.

Yan Bao, KIM IL BOM, Wenhai Li, Dongliang Zhang, Liye Gao, 2023: A detection method of segment misalignment and joint opening in metro shield tunnel ring based on point cloud. Urban Mass Transit, 26(09): 143-149. doi:10.16037/j.1007-869x.2023.09.025.

Fei Guo, Zhongliang Ai, Yan Bao, Heng Kong, Lejun Pei, 2023: Detection and analysis of segment misalignment and joint opening of subway shield tunnel based on point cloud data. Urban Mass Transit, 26(11): 25-30. doi:10.16037/j.1007-869x.2023.11.005

Beijing: China Planning Press, 2017: GB 50446-2017, Shield tunnel construction and acceptance specification.